Journal of Molecular Liquids 347 (2022) 118363

Contents lists available at ScienceDirect

Journal of Molecular Liquids

journal homepage: www.elsevier.com/locate/molliq

Molecular dynamics study on vibration-mode matching in surfactant-mediated thermal transport at solid–liquid interfaces

Hiroki Matsubara [a,*], Donatas Surblys [a], Yunhao Bao [a,b], Taku Ohara [a]

[a] Institute of Fluid Science, Tohoku University, 2-1-1 Katahira, Aoba-ku, Sendai 980-8577, Japan
[b] Department of Finemechanics, Graduate School of Engineering, Tohoku University, 2-1-1 Katahira, Aoba-ku, Sendai 980-8577, Japan

ARTICLE INFO

Article history:
Received 22 September 2021
Revised 1 December 2021
Accepted 17 December 2021
Available online 21 December 2021

Keywords:
Molecular dynamics simulation
Vibrational density of states
Surfactants
Solid-liquid interface
Thermal resistance
Thermal conductance

ABSTRACT

Surfactants have attracted attention as a means of enhancing thermal transport across solid–liquid interfaces. In the present study, non-equilibrium molecular dynamics simulation was used to study the effect of surfactants on interfacial thermal transport at solid–liquid interfaces, from the viewpoint of vibration-mode matching. The solid atom, surfactant molecule, and solvent molecule were all represented by a single atom. The vibrational characteristics of surfactant molecules were altered by changing surfactant mass m_{srf}, surfactant concentration c_{srf}, and the interaction strength between solid atoms and surfactant molecules, $\varepsilon_{sld-srf}$. For given values of c_{srf} and $\varepsilon_{sld-srf}$, the interfacial thermal resistance (ITR) between the solid and surfactant solution exhibited a minimum as a function of m_{srf}. This minimum was found to result from the mutual interference of interparticle heat transfer among atoms in the solid surface layer, and surfactant and solvent molecules in the first and second adsorption liquid layers. The amount of interparticle heat transfer was only partly correlated with the traditionally used overlap of vibrational density of states and with the matching of the characteristic frequencies associated with the spring constant of potential of mean force, proposed here. From this result, we conclude that ITR at solid–liquid interfaces can be minimized by optimizing the vibrational characteristics of surfactant molecules, but the theory of vibration-mode matching should be refined in order to fully identify the condition under which the best vibrational matching occurs between solid, surfactant, and solvent.

1. Introduction

The miniaturization of electronic devices such as power modules has led to a sharp increase in the density of heat generated from semiconductor components, and an efficient removal of the excess heat has become a vital concern in many industrial fields. A common way to improve heat dissipation in such devices is to insert thermal interface materials (TIMs) [1,2] between a high-heat-generating component and a heat sink. Since TIMs intend to fill the gap formed by imperfect contact of two rough surfaces with a highly thermally conductive material, liquid-like materials in which carbon or metal/metal oxide fillers are dispersed are typically used as TIMs. In order to maximize the performance of TIMs, it is necessary not only to increase intrinsic thermal conductivity of TIM, but also to increase the interfacial thermal conductance (ITC) or, equivalently, reduce the interfacial thermal resistance (ITR) between TIMs and solid surfaces.

Surfactants are widely used as additives in aqueous as well as non-aqueous solvents for various purposes including reduction of surface tension, modification of rheological properties, enhancement of oil recovery, and control of wettability and surface friction [3–6]. Both experimental and computational studies have shown [7–12] that surfactants can improve ITC between solids and liquids. On one hand, this effect of surfactant can be understood by its strong affinity with both solid surface and solvent. A number of molecular dynamics (MD) studies have found positive correlations between ITC and the affinity between solids and liquids, in view of interaction strength [13], surface charge [14], wetting/-work of adhesion [15,16], and surface roughness [17]. In addition, it has also been reported that ITC is correlated with the liquid structure near solid surfaces [18], which can affect ITC independently of the solid–liquid affinity [19,20]. In consistent with these studies, our MD studies of surfactant-mediated interfacial heat transfer [9,21–23] have revealed that the improvement of the solid–liquid affinity and the induction of interfacial liquid structuring are both important roles of surfactants in enhancing interfacial thermal transport.

* Corresponding author.
E-mail address: matsubara@microheat.ifs.tohoku.ac.jp (H. Matsubara).

https://doi.org/10.1016/j.molliq.2021.118363
0167-7322/

On the other hand, mechanism of interfacial thermal transport is often explored in view of vibrational modes. In particular, phonon conduction picture [24,25] implies a correlation between ITC and the overlap of vibrational density of states (VDOS) of two materials in contact [26]. This correlation is no more than a hypothesis because VDOS is different from the spectrum of heat flow itself, and a method for spectrally decomposing ITC at solid–liquid interfaces has become available [27]. Nevertheless, VDOS overlap is still widely used as a tool for understanding interfacial thermal transport. The correlation between interfacial thermal transport and VDOS overlap has been reported not only for solid–solid interfaces [28–30], but also for solid–liquid interfaces [31–36]. It was also suggested that temperature jump at a solid–liquid phase boundary of the same substance can disappear when a perfect vibrational coupling occurs [37]. Thus, the idea of vibration-mode matching seems to work at solid–liquid interfaces, even though phonon might not be suitable as a picture of thermal energy carrier in liquids.

In the present study, we consider the surfactant-mediated thermal transport from the viewpoint of vibration-mode matching. Non-equilibrium MD (NEMD) simulations were performed for the interface of a monatomic crystal and a surfactant solution composed of monatomic surfactant and solvent molecules. The vibrational characteristics of surfactant molecules were altered by changing surfactant mass, surfactant concentration, and the interaction strength between solid atoms and surfactant molecules. The total heat conduction at the interface was decomposed into the heat transfer among atoms in the solid surface layer, and the surfactant and solvent molecules in the first and second adsorption layers. For each pair of atoms and molecules, the correlation between the amount of interparticle heat transfer and the degree of vibration-mode matching was examined. In order to quantify the degree of vibration-mode matching, two approaches were examined here. One is VDOS overlap and the other is the matching of the characteristic frequencies associated with the spring constant of potential of mean force (PMF). PMF [38,39] is considered to be the effective pair potential of the two particles in a medium at finite temperature. If the medium is solid-like, it seems reasonable to assume that particles oscillate near the potential minimum and the associated vibrational frequency can be derived from the spring constant of the PMF. We call this frequency the characteristic frequency of PMF for short. In a liquid state, such vibration is not persistent, but an instantaneous reciprocating motion that occurs when two particles collide may be seen as part of this vibration, and the number of such collisions is quite large because statistically liquid molecules spend most of time near the minimum of PMF. In addition, it is known [40,41] that there is a correlation between thermal energy transfer due to pair interaction and PMF (or, equivalently, radial distribution function as will be explained later by Eq. (11)). Therefore, the matching in the characteristic frequencies of PMF is worth considering.

2. MD simulation

2.1. Molecular models and system details

The simulation system was consisted of two blocks of monatomic crystal sandwiching a surfactant solution as shown in Fig. 1(a). The solvent and surfactant molecules were both represented by a monatomic molecule in order to focus on the essential physics. The pair interaction between liquid molecules was expressed by Lennard-Jones (LJ) potential:

$$U_{\mathrm{LJ}}(r) = 4\varepsilon\left[\left(\frac{\sigma}{r}\right)^{12} - \left(\frac{\sigma}{r}\right)^{6}\right] \tag{1}$$

where r is interatomic distance, and ε and σ are energy and distance parameters, respectively. The potential parameters of argon [42], $\sigma = 3.405$ Å and $\varepsilon = 1.65 \times 10^{-21}$ J were used for all of solvent–solvent, solvent–surfactant, and surfactant–surfactant interactions. The mass of solvent molecule was set to m_{slv} = 39.95 u while for the surfactant mass m_{srf}, eleven cases from χ = 0.1 to 5.0 were considered in terms of the surfactant-to-solvent mass ratio $\chi = m_{\mathrm{srf}}/m_{\mathrm{slv}}$. The largest χ corresponds to the surfactant mass of m_{srf} = 199.75 u, which is nearly the same as the mass of the solid atom, m_{sld} = 195.08 u. The solid atoms were assumed to be platinum, and their pair interactions were described by Morse potential:

$$U_{\mathrm{Morse}}(r) = D\left[e^{-2\alpha(r-r_0)} - 2e^{-\alpha(r-r_0)}\right] \tag{2}$$

where we adopted the potential parameters of Pamuk and Halicioğlu [43]: D = 1.16214 × 10^{-19} J, r_0 = 2.91049 Å, and α = 1.62597 $Å^{-1}$.

The interaction between the solid atom and the solvent molecule was described by LJ potential and the parameters were chosen as $\sigma_{\mathrm{sld-slv}}$ = 2.935 Å and $\varepsilon_{\mathrm{sld-slv}} = 0.33 \times 10^{-21}$ J, which corresponds to a low wettability of argon droplet on platinum crystal surface with contact angle $\theta \sim 140°$ according to Spijker et al. [44] (They employed slightly different molecular models than ours.) For the solid–surfactant interaction, the distance parameter was the same as that of the solid–solvent interaction, but the energy parameter $\varepsilon_{\mathrm{sld-srf}}$ was set to be higher than $\varepsilon_{\mathrm{sld-slv}}$. In order to investigate the effect of the affinity between surfactant and solid surface, we examined the two cases, $\varepsilon_{\mathrm{sld-srf}} = \varepsilon_{\mathrm{low}} \equiv 1.25 \times 10^{-21}$ J and $\varepsilon_{\mathrm{sld-srf}} = \varepsilon_{\mathrm{high}} \equiv 5.00 \times 10^{-21}$ J, which corresponds to $\theta \sim 90^{\circ}$ and $\theta \sim 0^{\circ}$, respectively [44]. Hereafter, 'affinity' is used as the same meaning as the strength of interaction. The cut-off radius for all the interactions was set to be 12 Å.

The x and y dimensions of the simulation box were S_{xy} = 38.78 × 38.38 $Å^2$ and the periodic boundary conditions were applied while a fixed boundary condition was applied in the z direction by freezing the outermost solid atoms as will be described in Section 2.2. Each of the left and right crystal blocks was composed of 3136 atoms arranged in the face-centered cubic crystal of platinum, and the (1 1 1) face was in contact with the surfactant solution. One crystal block had 14 atomic layers along the z direction, each containing 224 atoms. The surfactant solution contained 1600 molecules as the sum of solvent and surfactant molecules. As shown in Fig. 1(b), the slab volume for the range $z_c - 10 \le z \le z_c + 10$ Å was defined as the liquid bulk region LB, where z_c is the center of the system in the z direction. The surfactant concentration c_{srf} was defined as the percentage of the number of surfactant molecules to the total number of liquid molecules in LB. To investigate the effect of surfactant concentration, we examined four cases: c_{srf} = 5%, 15%, 30%, and 50%, as well as the pure solvent case (c_{srf} = 0%). The method of controlling the surfactant concentration is described in Section 2.2.

2.2. Simulation procedures

LAMMPS software [45] was used for all MD simulations in the present study. The numerical integration of equation of motion was performed using velocity-Verlet algorithm with the simulation timestep of 0.5 fs. This timestep is sufficiently short for resolving the vibration of solid atoms and the dynamics of surfactant molecule with the smallest mass. The simulation procedure was composed of Phase 1–4 as described below.

2.2.1. Phase 1

This phase aimed to adjust pressure and surfactant concentration to given values under constant heat flux. As shown in Fig. 1

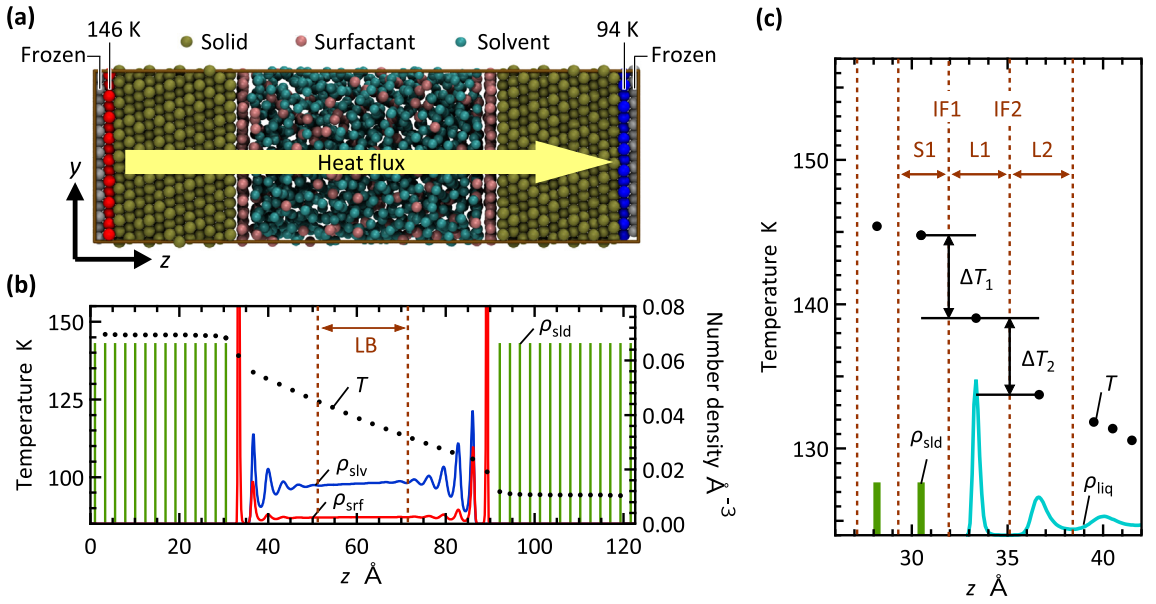

Fig. 1. (a) Snapshot of NEMD simulation system for the case with c_{srf} = 5%, χ = 1.0, and $\varepsilon_{sld-srf} = \varepsilon_{high}$. (b) The profiles of temperature T (left axis) and number density (right axis) of solid atoms (ρ_{sld}), solvent molecules (ρ_{slv}), and surfactant molecules (ρ_{srf}) corresponding to subfigure (a). The region denoted by LB is the liquid bulk region, where surfactant concentration c_{srf} is defined. (c) An enlarged view of subfigure (b) near the left solid–liquid interface, in order to show the locations of a solid layer S1, liquid adsorption layers L1 and L2, interfaces IF1 and IF2, and the definition of temperature jump ΔT_1 and ΔT_2, where $\rho_{liq} = \rho_{slv} + \rho_{srf}$ is the density of liquid molecules.

(a), a constant heat flux was imposed in the z direction by controlling the temperature of the second outermost atom layers in the left and right crystals to 146 K and 94 K, respectively, using the Langevin thermostat. While the outermost layer in the left crystal block was frozen, the atoms in the outermost layer in the right crystal were subject to a constant external force in the z direction corresponding to a pressure of 4.5 MPa. This method of pressure controlling faithfully mimics the pressure equilibration in practical systems and is one possible way when the system is not periodic in the direction of pressure control. This pressure condition was chosen so that the liquid molecules are in a liquid-like state, based on the fact that the critical point of the LJ fluid employed here as the solvent (argon) is approximately at 146 K and 4.5 MPa [42]. Our previous study confirmed [9] that with this temperature and pressure setting, no clear vaporization of liquid molecules occurs. We also note that the system was not relaxed to an equilibrium state before applying the temperature difference. In the present case, it is reasonably expected that our system composed of monatomic molecules is rarely trapped in a metastable basin of free energy, unlike the case of, e.g., long chain polymers. In such a case, the final non-equilibrium steady state is not significantly dependent on specific thermodynamic paths, and the relaxation to an equilibrium state is not always necessary. The phase-1 simulation was performed for 30 ns and was conducted for different values of c_{srf} and $\varepsilon_{sld-srf}$.

During the phase-1 simulation, surfactant concentration was adjusted to the target value c_{srf} in a dynamical manner. Before the simulation starts, the liquid molecules were all set to 'solvent' and were randomly arranged between the crystal blocks. For every 1000 steps, liquid molecules with a fraction c_{srf} were randomly picked from the bulk liquid region LB and were switched to 'surfactant' by artificially resetting their interaction parameter with solid atoms to $\varepsilon_{sld-srf}$, while the rest of molecules in LB were similarly reset to 'solvent'. At this stage, the surfactant and solvent molecules have the same mass. At the end of the simulation, the system reached a steady state, and the surfactant concentration in LB and the position of the outermost layer in the right crystal were nearly constant.

2.2.2. Phase 2

The outermost layer of the right crystal was fixed to its average position, which was obtained from the time average over the last 5 ns of phase 1, and the dynamical switching of liquid molecular type was turned off. The system was then relaxed for 10 ns.

2.2.3. Phase 3

The simulation for each c_{srf} and $\varepsilon_{sld-srf}$ further branched into 11 cases corresponding to different values of surfactant mass, m_{srf}. After the change of m_{srf}, the system was equilibrated for 30 ns. At the end of phase 3, the system was considered to reach a non-equilibrium steady state under constant heat flux for each set of c_{srf}, m_{srf}, and $\varepsilon_{sld-srf}$.

2.2.4. Phase 4

The production run was conducted for 100 ns to sample the data for analysis. The statistical error of a physical quantity was estimated from the standard error of mean over the five average values obtained by dividing the production run into five 20 ns segments.

2.3. Analysis of interfacial thermal transport and vibrational characteristics

The density and temperature profiles of the surfactant solution were calculated by dividing the system into slabs of a width Δz = 0.1 Å in the z direction, whereas those of the solid atoms were calculated layer by layer. As an example, the density and temperature profiles near the left interface for the case with χ = 1.0, c_{srf} = 15%, and $\varepsilon_{sld-srf} = \varepsilon_{high}$ are shown in Fig. 1(b). The density profile shows that in addition to the solid atom layers, the liquid molecules in the vicinity of the solid surface form adsorption layers. We considered interfaces of these layers at the midpoint of the peaks of two adjacent layers. Of these interlayer interfaces, only interface 1 (IF1) and interface 2 (IF2) shown in Fig. 1(c) were found to make a significant contribution to the total ITR at the left solid–liquid interface. Therefore, ITR at the left interface, R_{left}, was approximated as

$$R_{\text{left}} \sim R_1 + R_2 \tag{3}$$

where the ITR at interface I was calculated as

$$R_I = \Delta T_I / J_{\text{ext}} \tag{4}$$

Here, ΔT_1 is the temperature difference between the surface solid layer S1 and the first adsorption layer L1, and ΔT_2 is that between L1 and the second adsorption layer L2. ITR was thus calculated based on the temperature of the atom and molecular layers on both sides of the interface. This definition is somewhat different from the commonly used one where linear temperature profiles in the solid and liquid sides are extrapolated to the interface position to calculate the temperature difference [26]. However, for the present purpose of analyzing interfacial heat transfer and vibration-mode matching layer by layer, it is considered to be more rigorous to use the actual layer temperature, rather than the extrapolated one.

The value of externally applied heat flux J_{ext} was calculated as

$$J_{\text{ext}} = \left\langle \dot{E}_+ - \dot{E}_- \right\rangle / (2S_{xy}) \tag{5}$$

where $\langle \ldots \rangle$ means the time average, and $\dot{E}_+ > 0$ and $\dot{E}_- < 0$ are the rates of energy injection per unit time from the Langevin thermostats coupled with the left and right crystals, respectively. The ITR at the right interface, R_{right}, was similarly computed, and the average of R_{left} and R_{right} was calculated as

$$R_{\text{ave}} = (R_{\text{left}} + R_{\text{right}})/2 \tag{6}$$

In the present study, the detailed analysis of interfacial thermal transport and vibration-mode matching was performed only for the left interface, since R_{left} and R_{right} showed similar dependences on χ, c_{srf}, and $\varepsilon_{\text{sld-srf}}$. To analyze the molecular-scale heat transfer, the z component of the internal heat flux across an interlayer interface I, J_I, was calculated using the method of planes (MoP) formalism as [46,47]

$$J_I S_{xy} = \left\langle \sum_i e_i v_{z,i} \delta(z_i - z_I) \right\rangle + \left\langle \frac{1}{4} \sum_i \sum_{j \neq i} \mathbf{f}_{ij} \cdot \mathbf{v}_i \left[sgn(z_i - z_I) - sgn(z_j - z_I) \right] \right\rangle \tag{7}$$

where $e_i = m_i \mathbf{v}_i^2/2 + (1/2)\sum_j U_{ij}$, m_i, $\mathbf{v}_i$, $v_{z,i}$, and z_i are the mechanical energy, mass, velocity vector, the z component of velocity, and the z position of atom i, respectively; U_{ij} is the interaction potential between atoms i and j and $\mathbf{f}_{ij} = -\partial U_{ij}/\partial \mathbf{r}_i$ is the corresponding force on atom i; z_I is the z position of the interface I; sgn (z) is the sign of z. The Dirac delta function was approximated as $\delta(z_i - z_I) \sim \left[\theta(z_i^+ - z_I) - \theta(z_i^- - z_I)\right]/(z_i^+ - z_i^-)$, where $\theta(z)$ is the Heaviside step function, i.e., $\theta(z) = 1$ if $z > 0$ and $\theta(z) = 0$ otherwise; $z_i^\pm = z_i \pm v_{z,i}\Delta t/2 + f_{z,i}\Delta t^2/(4m_i)$ are the z_i at a half timestep earlier and later than the current timestep; Δt is the timestep; and $f_{z,i}$ is the z component of force on atom i. The first term in Eq. (7) is due to the atoms and molecules crossing the interface and is referred to as the particle transport term. On the other hand, the second term comes from the interactions across the interface and is called the interaction term.

The two interfaces IF1 and IF2 divide the left solid–liquid interface into three spatial domains: S1, L1, and L2. The partial heat flux, J_X, which represents a partial contribution to J_I from specific atom pairs in specific spatial domains, can be obtained by restricting i and j in the summations in Eq. (7) to these atoms. It is known that the direct heat transfer due to the van der Waals force can only reach the first neighbor molecules [40]. Therefore, only the atoms in the two layers making interface I can contribute to J_I. For example, in the case of the system shown in Fig. 1, the applied heat flux calculated by Eq. (5) was J_{ext} = 424 ± 6 MW/m^2. The heat flux between S1 and L1 was calculated as 418 ± 1 MW/m^2 and that between L1 and L2 as 416 ± 1 MW/m^2, which are almost equal to the total heat flux across IF1 and IF2, respectively. With this fact in mind, the ITR at IF1 was decomposed in terms of partial ITC $G_X = -J_X / \Delta T_I$ as

$$1/R_1 = G_1 = G_{1,\text{trans}} + G_{\text{sld1-srf1}} + G_{\text{sld1-slv1}} \tag{8}$$

where $G_{1,\text{trans}}$ is the particle transport term, and G_{AB} is the partial ITC due to the interaction between the two particle groups A and B, and the subscripts sld1, srf1, and slv1 denote the solid atoms in S1, surfactant molecules in L1, and solvent molecules in L1, respectively. The ITR at IF2 was similarly decomposed as

$$1/R_2 = G_2 = G_{2,\text{trans}} + G_{\text{srf1-srf2}} + G_{\text{srf1-slv2}} + G_{\text{slv1-srf2}} + G_{\text{slv1-slv2}} \tag{9}$$

where subscripts srf2 and slv2 are the surfactant and solvent molecules in L2, respectively.

As for the vibrational characteristics, VDOS was calculated by the Fourier transform of the mass-weighted velocity autocorrelation function as [48],

$$P(\nu) = C \sum_i m_i \int \langle \mathbf{v}_i(t) \cdot \mathbf{v}_i(0) \rangle e^{-2\pi i \nu t} dt \tag{10}$$

where ν is frequency and C is the normalization constant to ensure $\int P(\nu) d\nu = 1$. This normalized VDOS profile $P(\nu)$, which is effectively seen as the probability distribution of a single normal mode, was evaluated for each particle type and each region in Fig. 1(c). The overlap area O_{A-B} between two VDOS profiles $P_A(\nu)$ and $P_B(\nu)$ was calculated by [28,31] $O_{AB} = \int \min[P_A(\nu), P_B(\nu)] d\nu$, where $\min[P_A(\nu), P_B(\nu)]$ is the smaller of $P_A(\nu)$ and $P_B(\nu)$.

The characteristic frequency of PMF was derived as follows. For an interacting pair of particles A and B, the curve of PMF, $w_{AB}(r)$,

Table 1
Target surfactant concentration c_{srf}, number density of liquid molecules, $\rho_{\text{liq}} = \rho_{\text{srf}} + \rho_{\text{slv}}$, and actual surfactant concentration $c_{\text{srf}}^* = \rho_{\text{srf}}/\rho_{\text{liq}}$ at the bulk liquid region (LB), and ρ_{liq} and c_{srf}^* in the first adsorption layer (L1). Here, ρ_{srf} and ρ_{slv} are the number density of surfactant and solvent molecules, respectively. The values of ρ_{liq} and c_{srf}^* are the average over the simulations for different surfactant-to-solvent mass ratio, and those for L1 are further averaged over the left and right interfaces. The figure in the parentheses denotes the standard deviation of the last digit.

LB			L1	
c_{srf} %	ρ_{liq} 1/Å^3	c_{srf}^* %	ρ_{liq} 1/Å^3	c_{srf}^* %
5	0.01736(6)	5.0(2)	0.0125(3)	38(2)
15	0.0174(2)	15.6(5)	0.0153(2)	67.9(4)
30	0.0173(3)	31(1)	0.0169(3)	83(1)
50	0.01720(9)	50.1(3)	0.0177(2)	91.6(3)
5	0.01702(4)	5.6(1)	0.0256(2)	99.989(1)
15	0.01719(4)	13.9(1)	0.0257(2)	99.9962(8)
30	0.01713(3)	30.37(7)	0.02599(2)	99.9986(2)
50	0.01719(2)	46.89(6)	0.02602(2)	99.9994(1)

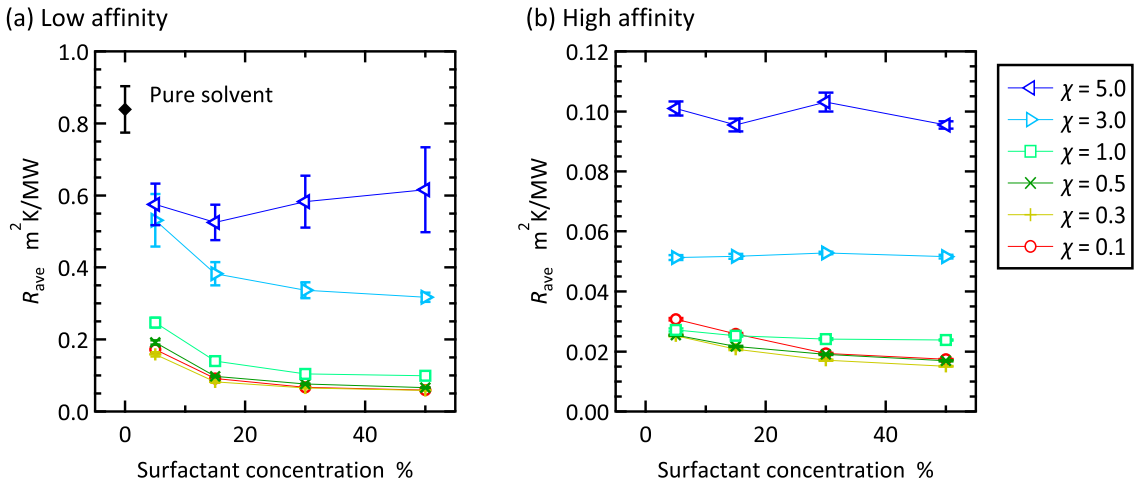

Fig. 2. Average of thermal resistance values at the left and right solid–liquid interfaces for the (a) low and (b) high solid–surfactant affinity cases, plotted as a function of surfactant concentration for each surfactant-to-solvent mass ratio χ.

was calculated from the radial distribution function $g_{AB}(r)$ as [38,39]

$$w_{AB}(r) = -k_B T_{AB} \ln g_{AB}(r) \tag{11}$$

where k_B is the Boltzmann constant and T_{AB} is temperature. As in the case of partial ITCs, each of particles A and B is assumed to be located in S1, L1, or L2. The radial distribution function between local volumes was computed using the method of Ref. [49], and the temperature in Eq. (11) was approximated as $T_{AB} = (T_{S1} + T_{L1})/2$ and $T_{AB} = (T_{L1} + T_{L2})/2$ for the A–B pairs interacting across IF1 and IF2, respectively, where T_{S1}, T_{L1}, and T_{L2} are the average temperature of S1, L1, and L2, respectively. The curve of PMF near the first minimum was fitted by a harmonic potential $k_{AB}(r-r_{min,AB})^2/2$ to determine the spring constant k_{AB} and the equilibrium position $r_{min,AB}$, from which the characteristic frequency of PMF was derived as

$$f_{AB} = \frac{1}{2\pi}\sqrt{\frac{k_{AB}}{\mu_{AB}}} \tag{12}$$

where $\mu_{AB} = m_A m_B/(m_A + m_B)$ is the reduced mass. The fitting was performed for the range $r_{min,AB} - \Delta r \le r \le r_{min,AB} + \Delta r$, and Δr was set to 1.5 Å except that Δr = 3.0 Å was used for the solid–solvent pair since the minimum of the PMF was rather broad.

3. Results and discussions

3.1. Liquid density

In Table 1, the liquid density ρ_{liq} and surfactant concentration c_{srf}^* measured during the production run in LB and those in L1 averaged over the left and right interfaces are summarized for each target surfactant concentration c_{srf} and solid–liquid affinity $\varepsilon_{sld-srf}$. Since change in the surfactant mass did not significantly alter the density profiles of solvent and surfactant molecules, the average values over the simulations with different values of m_{srf} were listed for each c_{srf} and $\varepsilon_{sld-srf}$. As denoted by the figure in the parentheses, the standard deviation due to different m_{srf} values is less than 1% and 5% for ρ_{liq} and c_{srf}^* in LB, respectively, and less than 2% and 4% for ρ_{liq} and c_{srf}^* in L1, respectively. The insensitivity of liquid structure to the variation of molecular mass was also reported by Ge and Chen [36]. The surfactant concentration c_{srf}^* in LB is close to the target value c_{srf}, indicating that the scheme of controlling surfactant concentration was successful.

As has been observed in past studies [9,21] and is demonstrated in Fig. 1(b), surfactant molecules are preferentially adsorbed on the solid surface according to their higher affinity

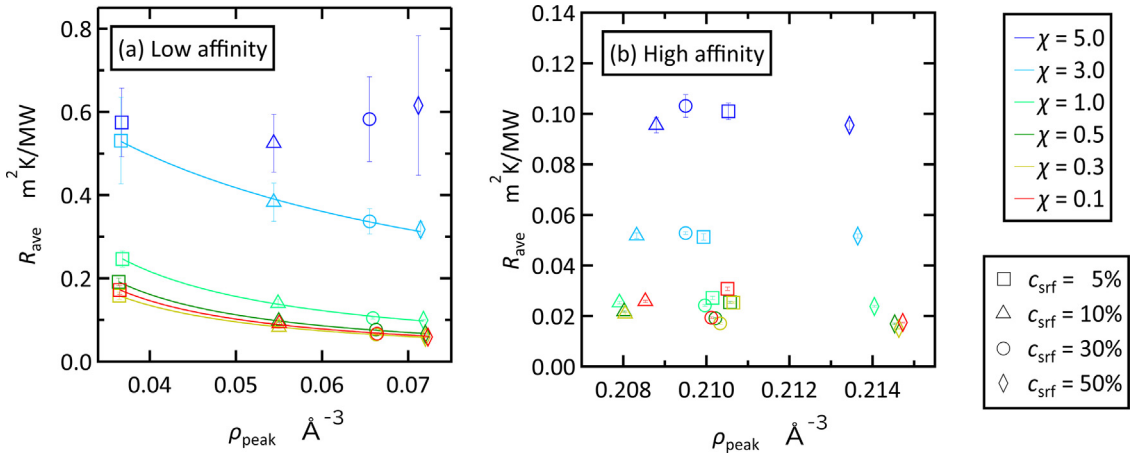

Fig. 3. Interfacial thermal resistance as a function of the density peak of the first adsorption layer, plotted for various values of surfactant-to-solvent mass ratio χ and surfactant concentration c_{srf}. Subfigures (a) and (b) are the results for the low and high solid–surfactant affinity cases, respectively. The solid curve represents the fitting with the rational function in Eq. (13) for each value of χ.

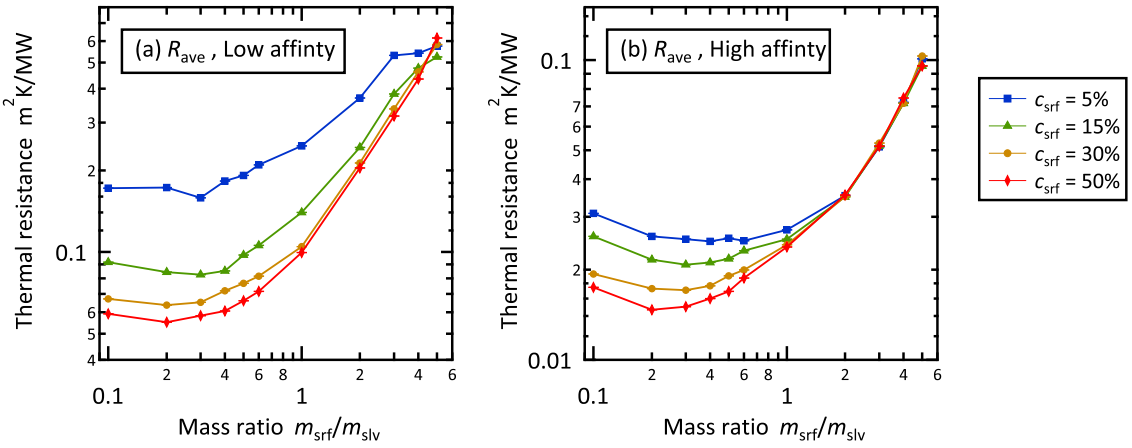

Fig. 4. (a) Interfacial thermal resistance averaged over the left and right solid–liquid interfaces, R_{ave}, plotted as a function of surfactant-to-solvent mass ratio for each surfactant concentration c_{srf}. Subfigures (a) and (b) are the results for the low and high solid–surfactant affinity cases, respectively.

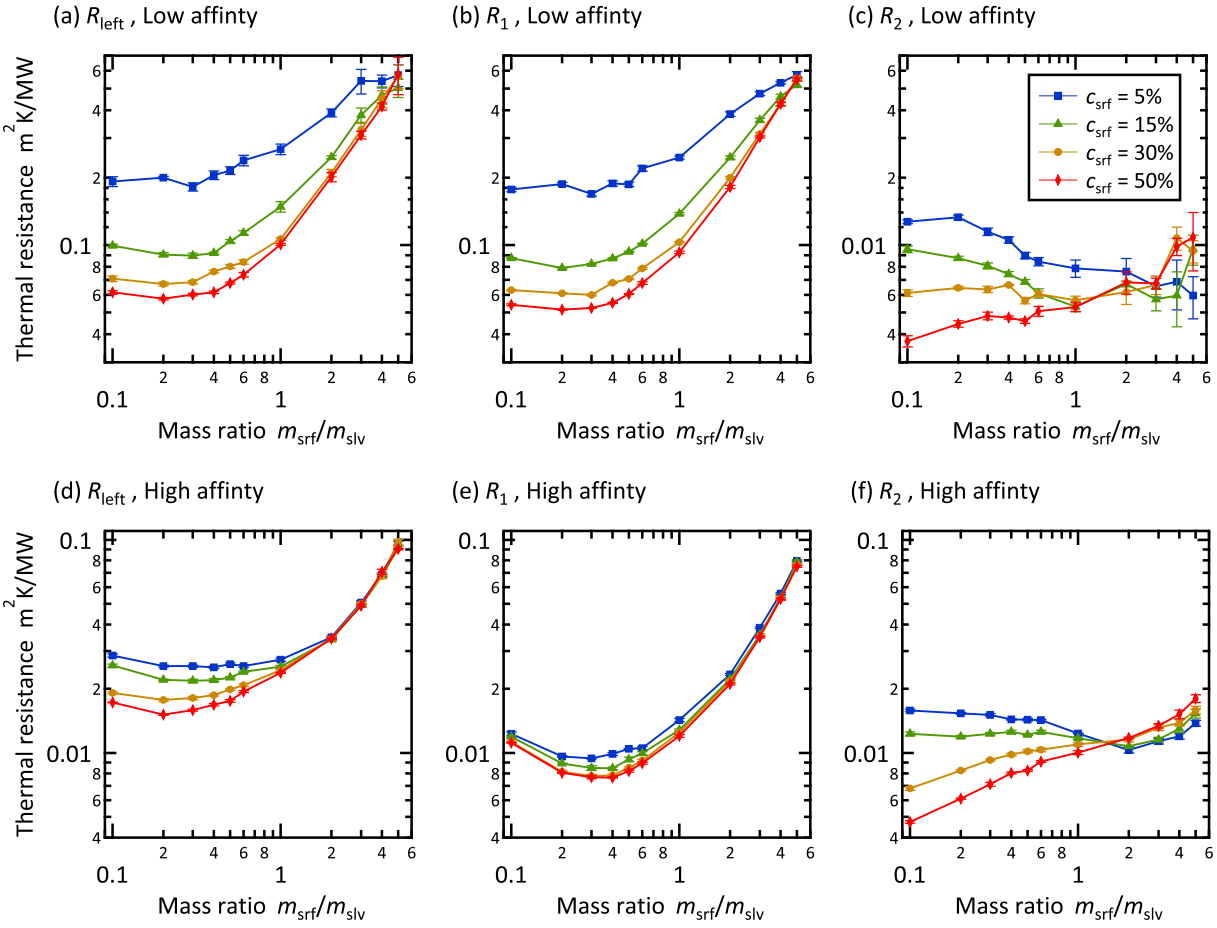

Fig. 5. (a) Total thermal resistance $R_{left} \sim R_1 + R_2$, (b) thermal resistance at IF1, R_1, and (c) that at IF2, R_2, for the low solid–surfactant affinity case with respect to the left solid–liquid interface. The curve for each surfactant concentration c_{srf} is plotted as a function of surfactant-to-solvent mass ratio. Subfigures (d), (e), and (f) are the same as (a), (b), and (c), respectively, for the high affinity case. The location of interfaces IF1 and IF2 are illustrated in Fig. 1(c).

to the solid atoms than that of solvent molecules. The surfactant concentration in L1 increases with increasing c_{srf} and $\varepsilon_{sld-srf}$, and consequently L1 is mostly occupied by surfactant molecules except for a few cases with low affinity and low c_{srf}. For the high affinity case, L1 contains almost no solvent molecule regardless of the value of c_{srf}.

3.2. Total ITR

In Fig. 2, the average ITR, R_{ave}, calculated by Eq. (6) is plotted as a function of surfactant concentration c_{srf} for each value of the mass ratio χ. All cases containing surfactant molecules have a lower value of R_{ave} than that in the pure solvent case, R_{ave} = 0.84

± 0.06 m^2K/MW. When compared at the same mass ratio, R_{ave} is lower for larger values of c_{srf} and $\varepsilon_{sld-srf}$, except some cases of high values of χ (χ = 5.0 for the low affinity and $\chi \geq 1.0$ for the high affinity), where the c_{srf} dependence is not clear within the statistical error. Such effect of surfactant concentration and solid–liquid affinity on ITR is similar to what has been reported in other MD studies [8,9,21].

MD studies on the graphene–water interface have reported [14,18] that when ITR is plotted as a function of the density peak of the first adsorption layer, ρ_{peak}, the curves for different wettability and pressure conditions collapse onto a single rational function of the form

$$R_{ave} = A/\left(\rho_{peak} + B\right) \tag{13}$$

where A and B are fitting parameters. We examined this relation for our systems and the result is displayed in Fig. 3, where ρ_{peak} is the average of the first adsorption peaks at the left and right interfaces. The fitting curve is also plotted for each mass ratio χ, only if the result is well described by Eq. (13). For the low affinity case (Fig. 3(a)), the different curves for $\chi \leq 0.5$ can be well represented by a single rational function as reported in Refs. [14,18]. However, as χ increases, the curve deviates from the master curve. For the high affinity case (Fig. 3(b)), the peak height did not change significantly with surfactant concentration, and it was difficult to see if the relation holds or not because R_{ave} is insensitive to the small change in the peak height. Thus, the inverse relation between R_{ave} and ρ_{peak} might hold also in the present systems, but the relation is not described by a single master curve when surfactant mass is large.

As demonstrated in Figs. 2 and 3, the ITR is significantly affected by the surfactant mass. This mass dependence should be attributed to the change in the vibrational characteristics, since the liquid structure was almost unchanged by the variation of surfactant mass as discussed in Section 3.1. When the ITR for each surfactant concentration is plotted as a function of the mass ratio, the curve shows a minimum at a certain value of χ, as shown in Fig. 4. When c_{srf} is 5%, the minimum is located at χ = 0.3 and $\chi \sim 0.4$ at the low and high affinity cases, respectively, and the location appears to slightly shift to a lower value when c_{srf} increases up to 50%.

As can be seen by comparing Fig. 5(a) and (d) with Fig. 4(a) and (b), respectively, the ITR of the left solid–liquid interface, R_{left}, shows quite a similar result to R_{ave}. Therefore, in the following investigation, we will focus on the left interface and perform the detailed analysis on interfacial heat transfer and vibration-mode matching. In Fig. 5(b) and (c), the χ dependence of R_{left} in the low affinity case was decomposed into those of R_1 and R_2, respectively, according to Eq. (3), and those in the high affinity case are shown in Fig. 5(e) and (f), respectively. The curves for the low affinity case are noisier than those for the high affinity case because of the large statistical error due to the low heat flux values. It is clearly shown for both affinity cases that R_1 determines the overall trend of R_{left} while R_2 slightly shifts the minimum position of R_{left} from that of R_1. However, it should be noted that in the low affinity case, R_1 is much higher than R_2 whereas in the high affinity case, R_1 and R_2 are comparable for most values of χ as a result of the significant decrease in R_1. The origin of the curve shapes for R_1 and R_2 will be discussed in more detail in Section 3.3.

3.3. Decomposition of ITR at each interface

The molecular-scale building blocks of R_1 were examined by decomposing the corresponding ITC $G_1 = 1/R_1$ into the partial ITCs according to Eq. (8). For each surfactant concentration, the partial ITCs are plotted as a function of χ in Fig. 6. For all cases, no particle passed through IF1 and therefore the particle transport term $G_{1,trans}$

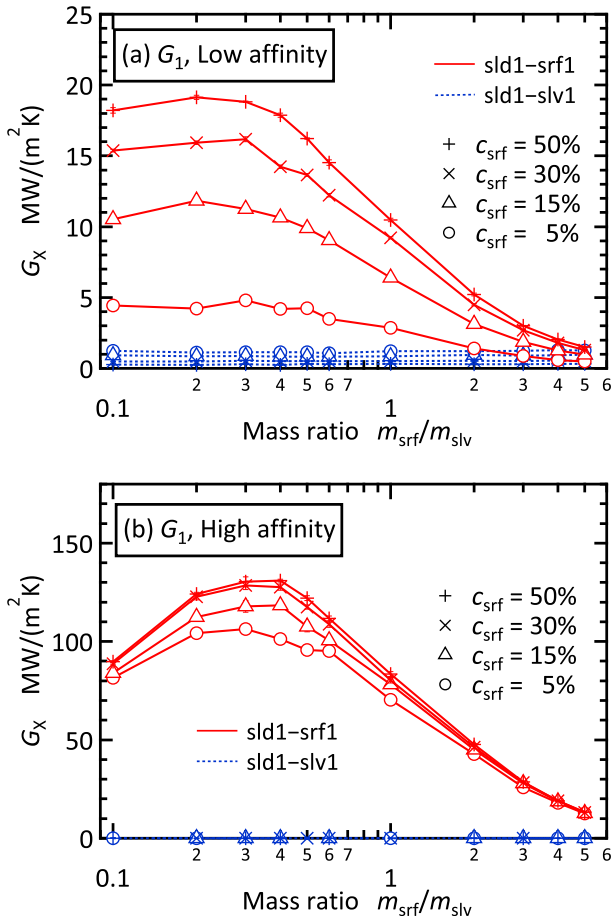

Fig. 6. Decomposition of thermal conductance at IF1, G_1, into the molecular-scale contributions from the interactions among solid atoms in S1 (sld1), surfactant molecules in L1 (srf1), and solvent molecule in L1 (slv1). The curves for each surfactant concentration c_{srf} are plotted as a function of surfactant-to-solvent mass ratio. Subfigures (a) and (b) are the results for the high and low solid–surfactant affinity cases, respectively. The locations of layers S1 and L1 and interface IF1 are illustrated in Fig. 1(c).

was zero. The contribution of the solid–surfactant interaction, $G_{sld1-srf1}$, dominates G_1, and thus the minimum position of R_1 corresponds to the peak position of $G_{sld1-srf1}$. This result is somewhat expected since L1 is mostly composed of surfactant molecules.

Similarly, the decomposition of G_2 at IF2 according to Eq. (9) is shown in Fig. 7. The result for the low affinity case is shown in Fig. 7(a) and (b), where the results for $\chi \geq 4.0$ are excluded because the statistical error was too large for the data to be physically meaningful. As shown in Fig. 7(b), the particle transport term $G_{2,trans}$ makes only a minor contribution to G_2, since the layer-to-layer migration of a molecule occurs only occasionally. The contribution of $G_{slv1-srf2}$ is even smaller owing to the lack of relevant molecular pairs. Therefore, the remaining components determine G_2 and R_2. The contributions of the interactions between homogeneous molecular pairs, $G_{srf1-srf2}$ and $G_{slv1-slv2}$ in Fig. 7(a), are nearly monotonically dependent on χ whereas that of heterogeneous pair, $G_{srf1-slv2}$ in Fig. 7(b), appears to have a peak around χ = 1, where the surfactant and solvent molecules have the same mass. As shown in Fig. 7(c) and (d), the partial ITCs for the high affinity case exhibit similar features to those for the low affinity case, but, different from the low affinity case, the peak position of $G_{srf1-slv2}$ is located at χ = 2 as shown in Fig. 7(d). The deviation of the peak position from χ = 1 indicates that the effective interaction between the surfactant molecules in L1 and the solvent molecules in L2 is different from the surfactant–solvent interaction in the

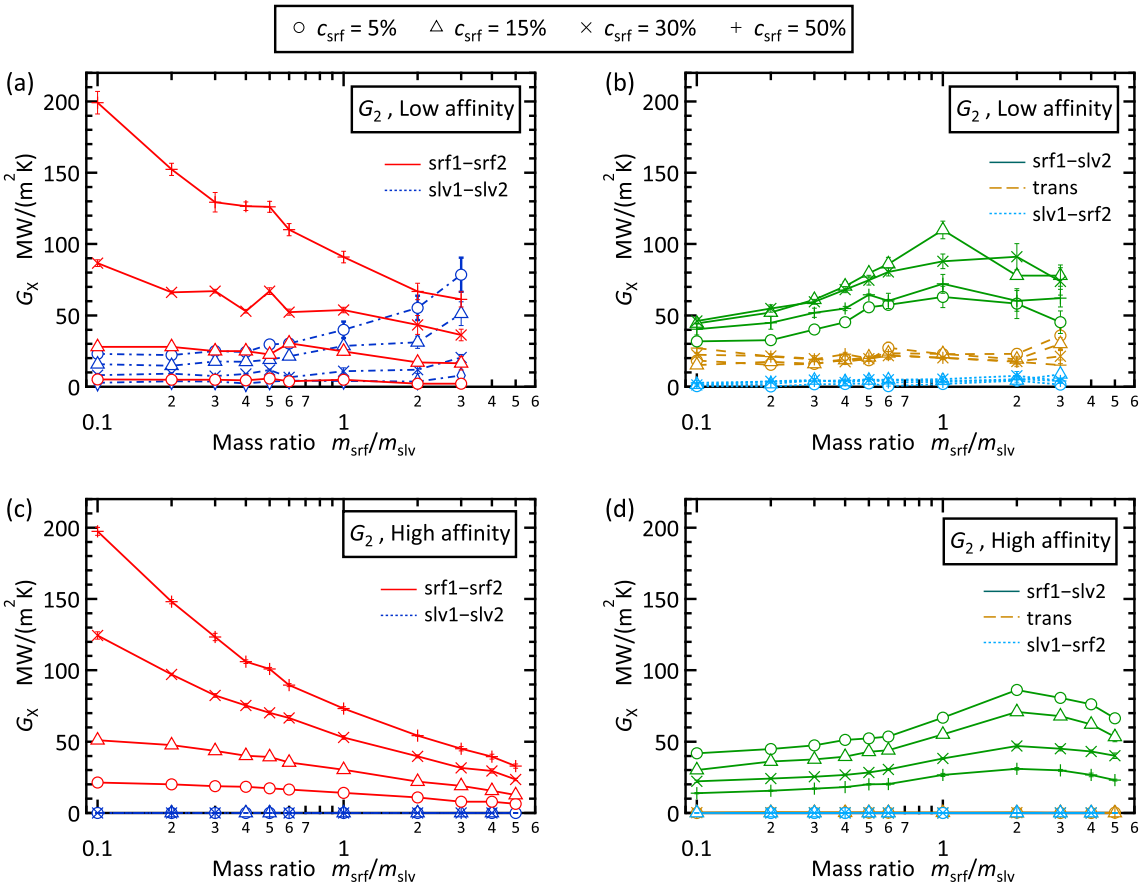

Fig. 7. Decomposition of thermal conductance at IF2, G_2, into the molecular-scale contributions from particle transport (trans) and interactions among surfactant molecules in L1 (srf1) and L2 (srf2) and solvent molecules in L1 (slv1) and L2 (slv2). The curves for each surfactant concentration c_{srf} are plotted as a function of surfactant-to-solvent mass ratio. For the low solid–surfactant affinity case, the contributions from the interactions between homogeneous molecular pairs and other contributions are separately displayed in (a) and (b), respectively, for better visibility. The result for the high affinity case is similarly shown in (c) and (d). The locations of layers L1 and L2 and interface IF2 are illustrated in Fig. 1(c).

bulk liquid region LB. This difference is reasonable considering that the liquid structure in L1 is significantly different from that in LB owing to the effect of the strong solid–surfactant interaction.

The result in Fig. 7 demonstrates that the complex behavior of R_2 in Fig. 5(c) and (f) results from the interference between $G_{srf1-srf2}$, $G_{slv1-slv2}$, and $G_{srf1-slv2}$, but the χ dependence of each component is relatively simple. The correlation between these partial ITCs and the vibrational characteristics of the relevant atoms and molecules will be investigated in Sections 3.4 and 3.5.

3.4. Overlap of vibrational density of states

An example of VDOS is displayed in Fig. 8, which is the result for the high affinity case with c_{srf} = 5%. The VDOS curves of surfactant molecules in L2 and L1 are shown by the solid curves in Fig. 8(a) and (b), respectively. It can be seen that the surfactant VDOS moves to the high-frequency side as χ decreases, and accordingly the degree of overlap with the VDOS of solvent molecules and that of solid atoms dramatically changes. We note that the VDOS curves of solvent molecules and solid atoms included in the figure are those for χ = 1, but almost the same curves are obtained for different values of χ. In L2, as shown in Fig. 8(a), the VDOS of surfactant molecules for χ < 1 is characterized by a single peak. The peak is likely because a surfactant molecule, which is lighter than solvent in this case, can vibrate for a while inside a cage temporarily formed by the surrounding solvent molecules. Differently from that in L2, the VDOS profile of surfactant molecules in L1 is a superposition of two peaks. The decomposition of Eq. (10) into the x, y, and z components showed that the lower peak or shoulder at the lower frequency side is originated from the vibration in the x and y directions, while the higher peak from the vibration in the z direction.

The overlap of VDOS profiles for each A–B pair is shown in Fig. 9 as a function of χ. It can be seen that as a whole, the change in VDOS overlap by varying surfactant concentration c_{srf} is relatively small. In the following, the χ dependence of VDOS overlap is compared with the corresponding curve of the partial ITC shown in Figs. 6 and 7. Regarding IF1, the curves of O_{AB} (Fig. 9(a) and (c)) and G_{AB} (Fig. 6(a) and (b)) are well correlated even though the correlation is not perfect. In particular, for the high affinity case, the VDOS overlap and partial ITC for solid–surfactant pair, $O_{sld1-srf1}$ in Fig. 9(c) and $G_{sld1-srf1}$ in Fig. 6(b), respectively, are quite similar in the points that they have a single peak and decay with increasing χ, although the peak positions are slightly different: χ = 0.2 for $O_{sld1-srf1}$ and χ = 0.3–0.4 for $G_{sld1-srf1}$. However, for the low affinity case, the peak is not seen in $O_{sld1-srf1}$ in Fig. 9(a) whereas $G_{sld1-srf1}$ exhibits it, albeit blunt. Thus, the peak in $G_{sld1-srf1}$ seems to be located at the position of the best frequency matching, but VDOS overlap explains only a part of it.

The same conclusion can be derived for IF2. For the surfactant–surfactant pair, the correlation between the VDOS overlap $O_{srf1-srf2}$ (Fig. 9(b) and (d)) and the partial ITC $G_{srf1-srf2}$ (Fig. 7(a) and (c)) may not be so clear, although the weak χ dependence of $O_{srf1-srf2}$ is in accordance with that of $G_{srf1-srf2}$ when c_{srf} is low. On the other hand, for the surfactant–solvent pair, $O_{srf1-slv2}$ (Fig. 9(b) and (d)) is well correlated with $G_{srf1-slv2}$ (Fig. 7(b) and (d)) except that their peak positions are different in the high affinity case (Fig. 9(d)

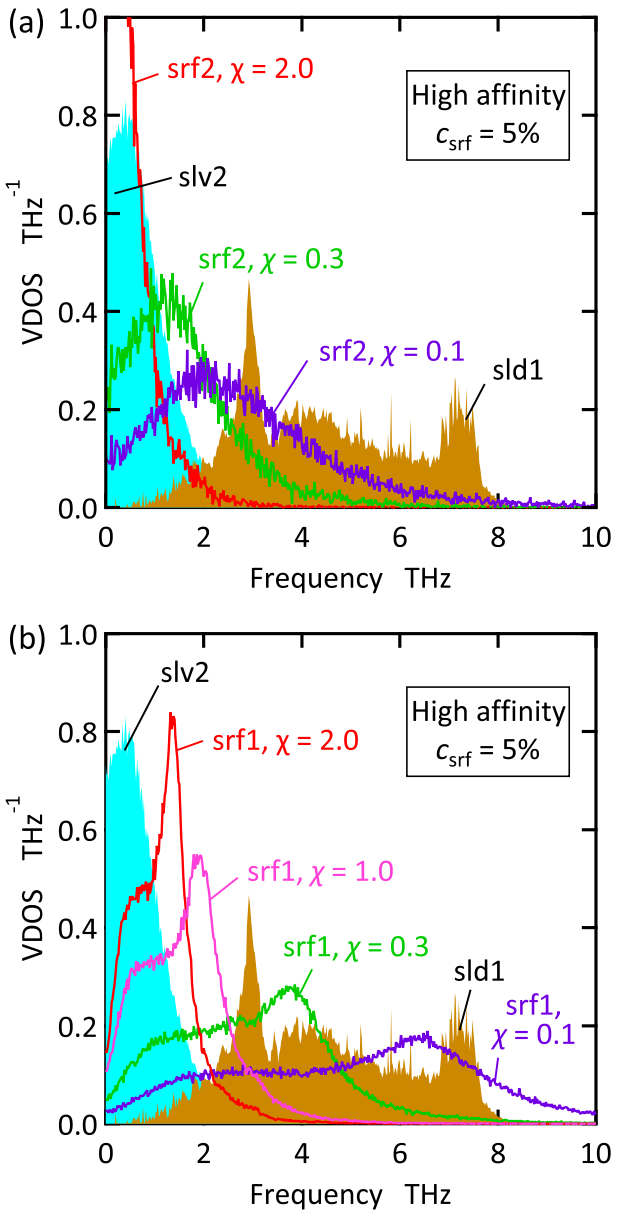

Fig. 8. (a) Vibrational density of states (VDOS) calculated for c_{srf} = 5% and $\varepsilon_{sld-srf} = \varepsilon_{high}$. The solid curves with different colors show the VDOS of surfactant molecules in L2 (srf2) for different surfactant-to-solvent mass ratio χ. The filled curves represent the VDOS of solvent molecules in L2 (slv2, cyan) and that of solid atoms in S1 (sld1, ochre) for χ = 1.0. (b) The same as (a) except that the solid curves are the VDOS of surfactant molecules in L1 (srf1). The locations of layers S1, L1, and L2 are illustrated in Fig. 1(c).

and 7(d)): χ = 3.0–4.0 for $O_{srf1-slv2}$ and χ = 2.0 for $G_{srf1-slv2}$. For the low affinity case, the peak position at χ = 1 may not be surprising since when χ = 1, a solvent molecule and a surfactant molecule are indistinguishable except the interaction strength with solid atoms, and also the effect of solid–surfactant interaction is relatively low for the low affinity case. Using NEMD simulation of LJ particles, Ge and Chen [36] also investigated the mass dependence of VDOS overlap at the solid–liquid interface by varying the mass of solid LJ particles, m_{sld}. In their cases of pure solid–liquid interface, thermal conductance monotonically increased with increasing m_{sld}, and the correlation between VDOS overlap and ITC was rather high. The result in the present study, however, demonstrates that when the particle mass dependence of ITC is not monotonic, the dependence is not explained solely by VDOS overlap.

3.5. Matching of characteristic frequencies of PMF

In Fig. 10, the PMF between two surfactant molecules in L1 and that between two solvent molecules in L2, both obtained for the high affinity case with c_{srf} = 5% and χ = 0.3, are depicted as an example. For ease of comparison, each PMF curve is shifted by a constant energy value so that the minimum energy is zero. Although the LJ potentials of the two pairs are the same, they exhibit different PMF curves because of the difference in liquid structure and molecular mass, and therefore the associated characteristic frequencies are different.

In Fig. 11, the characteristic frequency of PMF for each A–B pair, f_{AB}, is plotted as a function of χ. For each value of χ, the calculated values for different c_{srf}, indicated by different markers in Fig. 11, almost completely overlap, which means that the spring constant k_{AB} in Eq. (12) is independent of surfactant concentration. The χ dependence of f_{AB} is obtained if Eq. (12) is rewritten in terms of χ, which gives $2\pi f_{AB} = \sqrt{k_{AB}(m_A^{-1} + m_{slv}^{-1}\chi^{-1})}$ if B is surfactant, $2\pi f_{AB} = \sqrt{k_{AB}(m_B^{-1} + m_{slv}^{-1}\chi^{-1})}$ if A is surfactant, and f_{AB} is constant if A and B are not surfactant. The continuous curve in Fig. 11 represents this curve after fitting to the MD data with k_{AB} as a parameter.

Although not included in Fig. 11, the characteristic frequency of PMF for the solid–solid pair within S1, $f_{sld1-sld1}$, was almost independent of c_{srf}, χ, and $\varepsilon_{sld-srf}$, and the average over all simulation cases was $f_{sld1-sld1}$ = 5.190 THz with the standard deviation of 0.005 THz. Since the frequency of solid–surfactant pair across IF1, $f_{sld1-srf1}$, is monotonically decreasing with χ as shown in Fig. 11 (a) and (c), this frequency is closest to $f_{sld1-sld1}$ when χ = 0.1 for both low and high affinity cases. This value of χ is different from the peak position of $G_{sld1-srf1}$ in Fig. 6, χ = 0.3–0.4. Therefore, the peak position is not explained by the matching in the characteristic frequency of PMF. In solid-like states like S1 and L1, many kinds of phonon modes are involved in the heat transfer, and so it might be difficult to represent them by a single characteristic frequency.

In contrast, at IF2, Fig. 11(b) shows that for the low affinity case, the frequency matches between $f_{srf1-srf2}$, $f_{srf1-slv2}$, and $f_{slv1-slv2}$ at χ = 1 and this value of χ is equal to the peak position of $G_{srf1-slv2}$ in Fig. 7(b) except c_{srf} = 30%. In the high affinity case, the frequency for the surfactant–surfactant pair, $f_{srf1-srf2}$, is higher overall than in the low affinity case according to the higher spring constant $k_{srf1-srf1}$, while $f_{srf1-slv2}$ does not change significantly. As a result, the cross point of $f_{srf1-srf2}$ and $f_{srf1-slv2}$ shifts to χ = 2 as shown Fig. 11 (d). Again, this value of χ corresponds to the peak position of $G_{srf1-slv2}$ in Fig. 7(d). The result can be interpreted that when the characteristic frequency of PMF of surfactant–surfactant pair is equal to that of solvent–solvent pair, that of surfactant–solvent pair is also the same, and then, the partial ITC of the surfactant–solvent is maximized. Thus, PMF may provide a new frequency matching law at interfaces between liquid-like regions as IF2, although it does not work at interfaces of solid-like regions as IF1.

The exact reason for the minimum position of G_1 at χ = 0.3–0.4 was not very clear from the present result, even though VDOS overlap exhibited a peak at similar position. Zhang et al. [50] in their study of the scattering boundary method reported a peak behavior similar to ours for the ITC at the joint of two dissimilar one-dimensional harmonic chains. They found that the ITC is maximized when the spring constants satisfy $k_{12} = k_1k_2/(k_1 + k_2)$, where k_{12} is the spring constant of harmonic potential jointing the two chains, and k_1 and k_2 are the spring constants of the two chains. This rule is not applied to our case where the change in ITC is caused solely by m_{srf} without changing spring constants (the potential parameters of the constituent particles). Similar but slightly more complicated rules were also proposed for the case

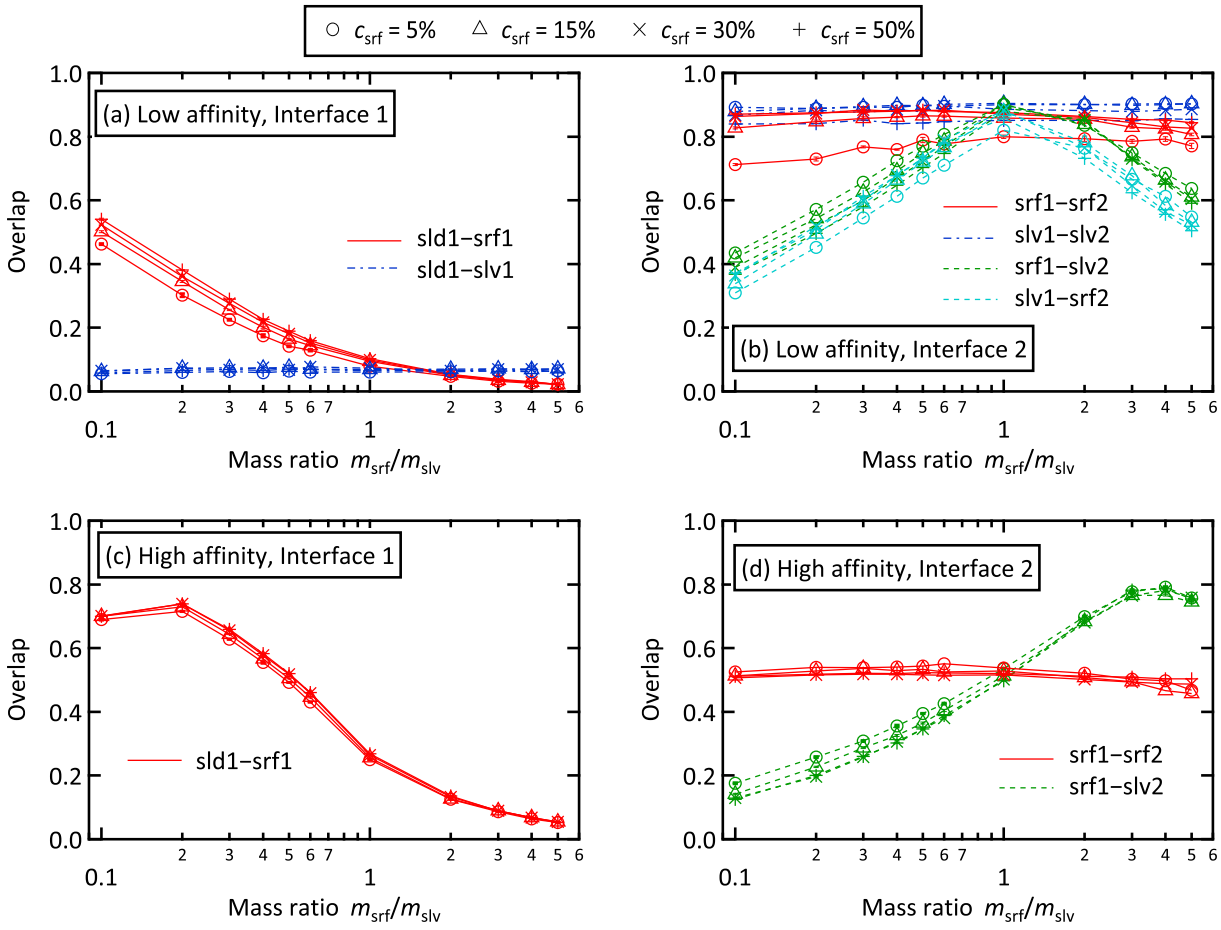

Fig. 9. VDOS overlap among solid atoms in S1 (sld1), solvent molecules in L1 (slv1) and L2 (slv2), and surfactant molecules in L1 (srf1) and L2 (srf2), plotted as a function of surfactant-to-solvent mass ratio for each surfactant concentration c_{srf}. (a) and (b) are the VDOS overlap across IF1 and F2, respectively, for the low solid–surfactant affinity case, while (c) and (d) are the same as (a) and (b), respectively, for the high affinity case. The locations of interfaces IF1 and IF2, and layers S1, L1, and L2 are illustrated in Fig. 1(c).

where a coupler chain is inserted between the two chains [51]. Saltonstall et al. also derived a simple expression for the transmission coefficient of a chain–coupler–chain system on the basis of non-equilibrium Green's function theory [52]. These rules predict that the ITC between two one-dimensional chains is maximized when the mass of the coupler particle is somewhere between those of the two chains. In contrast, in the present case, the value of m_{srf} that maximizes G_1 is smaller than both m_{slv} and m_{sld}. Thus, none of these rules explained the peak of G_1 in our three-dimensional case, but further studies on one-dimensional chain systems would be effective in finding the underlying mechanism of vibration-mode matching that is not captured by VDOS overlap and the characteristic frequency of PMF.

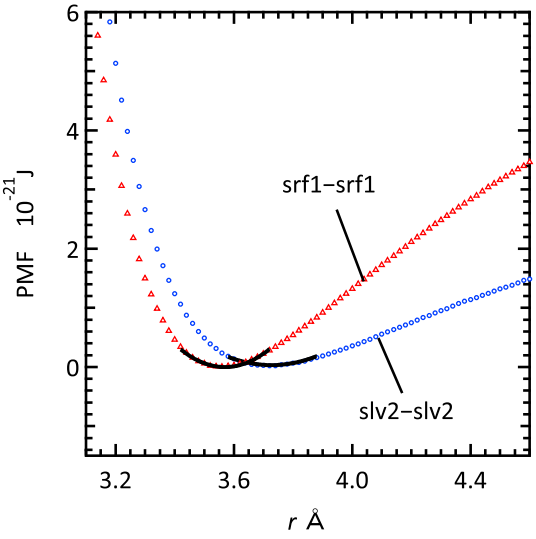

Fig. 10. Potential of mean force (PMF) as a function of intermolecular distance r for the surfactant molecules in L1 (red triangle) and that for the solvent molecules in L2 (blue circle), both calculated for c_{srf} = 5%, χ = 0.3, and $\varepsilon_{sld-srf} = \varepsilon_{high}$. The solid line near the minimum of PMF is the fitting curve based on a harmonic approximation. The locations of layers L1 and L2 are illustrated in Fig. 1(c).

In the present study, we mainly considered ITR at solid–liquid interfaces as one important factor that governs the performance of TIM. When trying to reduce the overall thermal resistance between two solid surfaces by inserting a surfactant solution as a TIM, one must also take the thermal conductivity in the bulk liquid region into account. It is expected that thermal conductivity of a typical surfactant solution has a similar nature to that of the ITC at the liquid–liquid interface IF2: that is, based on the partial ITCs in Fig. 7, the thermal conductivity is likely higher with decreasing surfactant mass and with increasing overlap in the characteristic frequency of PMF between solvent and surfactant molecules. On the other hand, since the characteristic frequency in solids in general is much higher than that in liquids, surfactants that maximize the vibrational matching with solvents are likely to have poor vibrational matching with solids. One must consider such a trade-off in selecting optimal surfactants that minimize the overall thermal resistance.

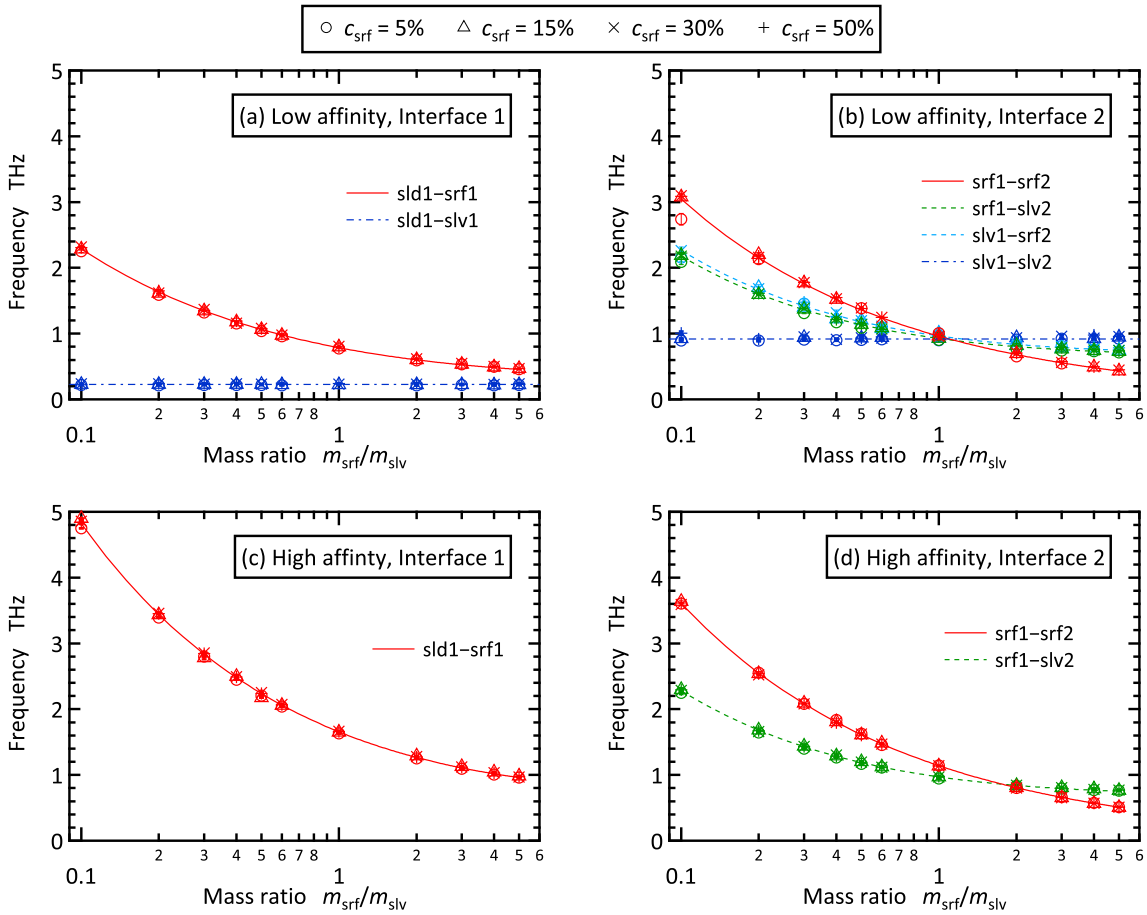

Fig. 11. Characteristic frequency of PMF for various pairs among solid atoms in S1 (sld1), solvent molecules in L1 (slv1) and L2 (slv2), and surfactant molecules in L1 (srf1) and L2 (srf2), plotted as a function of surfactant-to-solvent mass ratio. Different markers indicate different surfactant concentration c_{srf} while the continuous curve represents the fitting according to Eq. (12). (a) and (b) are the results for the particle pairs interacting across IF1 and IF2, respectively, both for the low solid–surfactant affinity case. (c) and (d) are the same as (a) and (b), respectively, for the high affinity case. The locations of interfaces IF1 and IF2 and layers S1, L1, and L2 are illustrated in Fig. 1(c).

4. Conclusions

In the present study, NEMD simulation was used to study the effect of surfactants on interfacial thermal transport at solid–liquid interfaces, from the viewpoint of vibration-mode matching. As the parameters to alter the vibration characteristics of surfactant molecules, surfactant concentration c_{srf}, solid–surfactant affinity $\varepsilon_{sld-srf}$, and the mass of surfactant in terms of surfactant-to-solvent mass ratio χ were considered.

For given values of c_{srf} and $\varepsilon_{sld-srf}$, the interfacial thermal resistance (ITR) at the solid–liquid interface was minimized when χ = 0.2–0.4. It was found that this minimum mainly comes from the ITR between solid surface layer and the first liquid adsorption layer, but also affected by that between the first and second adsorption layers. These layer-by-layer ITRs were decomposed into the contributions from molecular-scale heat transfer between atoms and molecules, and the decomposed components showed some correlations with the degree of vibration-mode matching, although the correlation was not perfect. In finding such correlations, the matching of the characteristic frequencies of potential of mean force was proved to be useful as a measure of vibration-mode matching in liquids, in addition to the conventionally used VDOS overlap.

The present result suggests that the minimum of ITR is determined by a certain kind of vibration-mode matching. It is therefore likely that ITR at solid–liquid interfaces can be minimized by optimizing the vibrational characteristics of surfactant molecules, but the theory of vibration-mode matching should be refined in order to fully identify the condition under which the best vibrational matching occurs between solid, surfactant, and solvent.

Declaration of Competing Interest

The authors declare that they have no known competing financial interests or personal relationships that could have appeared to influence the work reported in this paper.

Acknowledgments

This work was supported by JST CREST Grant Number JPMJCR17I2, Japan. Computational simulations were performed on the supercomputer system "AFI-NITY" at the Advanced Fluid Information Research Center, Institute of Fluid Science, Tohoku University.

References

[1] R.D. Pathumudy, K.N. Prabhu, Thermal interface materials for cooling microelectronic systems: present status and future challenges, J. Mater. Sci. Mater. Electron. 32 (9) (2021) 11339–11366, https://doi.org/10.1007/s10854-021-05635-w.

[2] J.S. Lewis, T. Perrier, Z. Barani, F. Kargar, A.A. Balandin, Thermal interface materials with graphene fillers: review of the state of the art and outlook for future applications, Nanotechnology 32 (14) (2021) 142003, https://doi.org/10.1088/1361-6528/abc0c6.

[3] M.A. Rahim, S. Mahbub, S.M.A. Ahsan, M. Alam, M. Saha, I. Shahriar, S. Rana, M. A. Halim, M.A. Hoque, D. Kumar, J.M. Khan, Conductivity, cloud point and molecular dynamics investigations of the interaction of surfactants with ciprofloxacin hydrochloride drug: effect of electrolytes, J. Mol. Liq. 322 (2021) 114683, https://doi.org/10.1016/j.molliq.2020.114683.
[4] N.K. Jha, M. Ali, S. Iglauer, M. Lebedev, H. Roshan, A. Barifcani, J.S. Sangwai, M. Sarmadivaleh, Wettability alteration of quartz surface by low-salinity surfactant nanofluids at high-pressure and high-temperature conditions, Energy Fuels 33 (8) (2019) 7062–7068, https://doi.org/10.1021/acs.energyfuels.9b01102.
[5] P. Zhou, J. Hou, Y. Yan, J. Wang, The effect of surfactant adsorption on surface wettability and flow resistance in slit nanopore: a molecular dynamics study, J. Colloid Interface Sci. 513 (2018) 379–388, https://doi.org/10.1016/j.jcis.2017.11.045.
[6] I.S. Chronakis, P. Alexandridis, Rheological properties of oppositely charged polyelectrolyte–surfactant mixtures: effect of polymer molecular weight and surfactant architecture, Macromolecules 34 (2001) 5005–5018, https://doi.org/10.1021/ma000609k.
[7] R. Lenin, P.A. Joy, C. Bera, A review of the recent progress on thermal conductivity of nanofluid, J. Mol. Liq. 338 (2021) 116929, https://doi.org/10.1016/j.molliq.2021.116929.
[8] L. Zhou, H. Ma, A molecular dynamics study on interfacial heat transport of alkanethiol surfactant coated nanofluids-effect of chain length and stiffness, Mol. Phys. 118 (2020), https://doi.org/10.1080/00268976.2020.1738580 e1738580.
[9] Y. Guo, D. Surblys, Y. Kawagoe, H. Matsubara, X. Liu, T. Ohara, A molecular dynamics study on the effect of surfactant adsorption on heat transfer at a solid-liquid interface, Int. J. Heat Mass Transf. 135 (2019) 115–123, https://doi.org/10.1016/j.ijheatmasstransfer.2019.01.131.
[10] X. Wu, Y. Ni, J. Zhu, N.D. Burrows, C.J. Murphy, T. Dumitrica, X. Wang, Thermal transport across surfactant layers on gold nanorods in aqueous solution, ACS Appl. Mater. Interfaces 8 (16) (2016) 10581–10589, https://doi.org/10.1021/acsami.5b1216310.1021/acsami.5b12163.s001.
[11] J. Park, D.G. Cahill, Plasmonic sensing of heat transport at solid-liquid interfaces, J. Phys. Chem. C. 120 (5) (2016) 2814–2821, https://doi.org/10.1021/acs.jpcc.5b11706.
[12] J. Huang, J. Park, W. Wang, C.J. Murphy, D.G. Cahill, Ultrafast thermal analysis of surface functionalized gold nanorods in aqueous solution, ACS Nano 7 (1) (2013) 589–597, https://doi.org/10.1021/nn304738u.
[13] G. Chen, J. Chen, Z. Wang, Thermal transport at interface between single-layer graphene and water film, Int. J. Thermophys. 41 (2020) 48, https://doi.org/10.1007/s10765-020-02629-4.
[14] Y. Ma, Z. Zhang, J. Chen, K. Sääskilahti, S. Volz, J. Chen, Ordered water layers by interfacial charge decoration leading to an ultra-low Kapitza resistance between graphene and water, Carbon N. Y. 135 (2018) 263–269, https://doi.org/10.1016/j.carbon.2018.04.030.
[15] N. Shenogina, R. Godawat, P. Keblinski, S. Garde, How wetting and adhesion affect thermal conductance of a range of hydrophobic to hydrophilic aqueous interfaces, Phys. Rev. Lett. 102 (2009) 1–4, https://doi.org/10.1103/PhysRevLett.102.156101.
[16] H. Acharya, N.J. Mozdzierz, P. Keblinski, S. Garde, How chemistry, nanoscale roughness, and the direction of heat flow affect thermal conductance of solid-water interfaces, Ind. Eng. Chem. Res. 51 (4) (2012) 1767–1773, https://doi.org/10.1021/ie2010274.
[17] D. Surblys, Y. Kawagoe, M. Shibahara, T. Ohara, Molecular dynamics investigation of surface roughness scale effect on interfacial thermal conductance at solid-liquid interfaces, J. Chem. Phys. 150 (2019) 1–11, https://doi.org/10.1063/1.5081103.
[18] D. Alexeev, J. Chen, J.H. Walther, K.P. Giapis, P. Angelikopoulos, P. Koumoutsakos, Kapitza resistance between few-layer graphene and water: liquid layering effects, Nano Lett. 15 (9) (2015) 5744–5749, https://doi.org/10.1021/acs.nanolett.5b03024.
[19] C.U. Gonzalez-Valle, B. Ramos-Alvarado, Spectral mapping of thermal transport across SiC-water interfaces, Int. J. Heat Mass Transf. 131 (2019) 645–653, https://doi.org/10.1016/j.ijheatmasstransfer.2018.11.101.
[20] C.U. Gonzalez-Valle, B. Ramos-Alvarado, Molecular dynamics simulations of wettability, thermal transport, and interfacial liquid structuring at the nanoscale in polar solid-liquid interfaces, ACS Appl. Nano Mater. 4 (4) (2021) 3821–3832, https://doi.org/10.1021/acsanm.1c00247.
[21] Y. Guo, D. Surblys, Y. Kawagoe, H. Matsubara, T. Ohara, A molecular dynamics study of heat transfer over an ultra-thin liquid film with surfactant between solid surfaces, J. Appl. Phys. 126 (18) (2019) 185302, https://doi.org/10.1063/1.5123583.
[22] Y. Guo, D. Surblys, H. Matsubara, Y. Kawagoe, T. Ohara, Molecular dynamics study on the effect of long-chain surfactant adsorption on interfacial heat transfer between a polymer liquid and silica surface, J. Phys. Chem. C. 124 (50) (2020) 27558–27570, https://doi.org/10.1021/acs.jpcc.0c08940.
[23] Y. Guo, D. Surblys, H. Matsubara, T. Ohara, A molecular dynamics study of the effect of functional groups and side chain on adsorption of alcoholic surfactant and interfacial thermal transport, J. Mol. Liq. 335 (2021) 116243, https://doi.org/10.1016/j.molliq.2021.116243.
[24] E.T. Swartz, R.O. Pohl, Thermal boundary resistance, Rev. Mod. Phys. 61 (3) (1989) 605–668.
[25] L.G.C. Rego, G. Kirczenow, Quantized thermal conductance of dielectric quantum wires, Phys. Rev. Lett. 81 (1) (1998) 232–235, https://doi.org/10.1103/PhysRevLett.81.232.
[26] Z. Liang, M. Hu, Tutorial: determination of thermal boundary resistance by molecular dynamics simulations, J. Appl. Phys. 123 (19) (2018) 191101, https://doi.org/10.1063/1.5027519.
[27] K. Sääskilahti, J. Oksanen, J. Tulkki, S. Volz, Spectral mapping of heat transfer mechanisms at liquid-solid interfaces, Phys. Rev. E. 93 (2016) 1–8, https://doi.org/10.1103/PhysRevE.93.052141.
[28] Z. Wang, A molecular dynamics study of the thermal transport in silicon/germanium nanostructures: from cross-plane to in-plane, Mater. Today Commun. 22 (2020) 100822, https://doi.org/10.1016/j.mtcomm.2019.100822.
[29] X. Zhang, J. Jiang, Thermal conductivity of zeolitic imidazolate framework-8: a molecular simulation study, J. Phys. Chem. C. 117 (36) (2013) 18441–18447, https://doi.org/10.1021/jp405156y.
[30] Z. Tian, K. Esfarjani, G. Chen, Enhancing phonon transmission across a Si/Ge interface by atomic roughness: first-principles study with the Green's function method, Phys. Rev. B - Condens. Matter Mater. Phys. 86 (2012) 1–7, https://doi.org/10.1103/PhysRevB.86.235304.
[31] X.-K. Chen, X.-Y. Hu, P. Jia, Z.-X. Xie, J. Liu, Tunable anisotropic thermal transport in porous carbon foams: the role of phonon coupling, Int. J. Mech. Sci. 206 (2021) 106576, https://doi.org/10.1016/j.ijmecsci.2021.106576.
[32] T. Zhou, H.K. Chilukoti, Z. Wu, F. Müller-Plathe, Effect of defects on the interfacial thermal conductance betweenn-heneicosane in solid and liquid phases and a graphene monolayer, J. Phys. Chem. C. 125 (25) (2021) 14149–14162, https://doi.org/10.1021/acs.jpcc.1c04676.
[33] S. Namsani, J.K. Singh, Enhancement of thermal energy transport across the gold-graphene interface using nanoscale defects: a molecular dynamics study, J. Phys. Chem. C. 122 (4) (2018) 2113–2121, https://doi.org/10.1021/acs.jpcc.7b0964310.1021/acs.jpcc.7b09643.s001.
[34] B.Y. Cao, J.H. Zou, G.J. Hu, G.X. Cao, Enhanced thermal transport across multilayer graphene and water by interlayer functionalization, Appl. Phys. Lett. 112 (2018) 1–5, https://doi.org/10.1063/1.5018749.
[35] Y. Wang, H.F. Zhan, Y. Xiang, C. Yang, C.M. Wang, Y.Y. Zhang, Effect of Covalent functionalization on thermal transport across graphene-polymer interfaces, J. Phys. Chem. C. 119 (22) (2015) 12731–12738, https://doi.org/10.1021/acs.jpcc.5b02920.
[36] S. Ge, M. Chen, Vibrational coupling and Kapitza resistance at a solid-liquid interface, Int. J. Thermophys. 34 (1) (2013) 64–77, https://doi.org/10.1007/s10765-012-1362-2.
[37] T.Q. Vo, B.H. Kim, Physical origins of temperature continuity at an interface between a crystal and its melt, J. Chem. Phys. 148 (2018) 3–8, https://doi.org/10.1063/1.5004545.
[38] J.G. Kirkwood, Statistical mechanics of fluid mixtures, J. Chem. Phys. 3 (5) (1935) 300–313, https://doi.org/10.1063/1.1749657.
[39] S.R.P. Bandlamudi, K.M. Benjamin, Communication: potentials of mean force study of ionic liquid ion pair aggregation in polar covalent molecule solvents, J. Chem. Phys. 148 (2018) 1–5, https://doi.org/10.1063/1.5028144.
[40] T. Ohara, Contribution of intermolecular energy transfer to heat conduction in a simple liquid, J. Chem. Phys. 111 (21) (1999) 9667–9672, https://doi.org/10.1063/1.480338.
[41] H. Matsubara, G. Kikugawa, T. Ohara, Comparison of molecular heat transfer mechanisms between water and ammonia in the liquid states, Int. J. Therm. Sci. 161 (2021) 106762, https://doi.org/10.1016/j.ijthermalsci.2020.106762.
[42] D.O. Dunikov, S.P. Malyshenko, V.V. Zhakhovskii, Corresponding states law and molecular dynamics simulations of the Lennard-Jones fluid, J. Chem. Phys. 115 (14) (2001) 6623–6631, https://doi.org/10.1063/1.1396674.
[43] H.Ö. Pamuk, T. Halicio??lu, Evaluation of morse parameters for metals, Phys. Status Solidi. 37 (2) (1976) 695–699.
[44] P. Spijker, A.J. Markvoort, S.V. Nedea, P.A.J. Hilbers, Computation of accommodation coefficients and the use of velocity correlation profiles in molecular dynamics simulations, Phys. Rev. E - Stat. Nonlinear, Soft Matter Phys. 81 (2010) 1–15, https://doi.org/10.1103/PhysRevE.81.011203.
[45] S. Plimpton, Fast parallel algorithms for short-range molecular dynamics, J. Comput. Phys. 117 (1) (1995) 1–19, https://doi.org/10.1006/jcph.1995.1039.
[46] B.D. Todd, P.J. Daivis, Nonequilibrium Molecular Dynamics, Cambridge University Press, Cambridge, 2017. doi: 10.1017/9781139017848.
[47] B.D. Todd, P.J. Daivis, D.J. Evans, Heat flux vector in highly inhomogeneous nonequilibrium fluids, Phys. Rev. E. 51 (5) (1995) 4362–4368, https://doi.org/10.1103/PhysRevE.51.4362.
[48] M.T. Dove, Introduction to Lattice Dynamics, Cambridge University Press, New York, 1993. doi: 10.1017/CBO9780511619885.
[49] Y. Kawagoe, D. Surblys, H. Matsubara, G. Kikugawa, T. Ohara, Cross-plane and in-plane heat conductions in layer-by-layer membrane: molecular dynamics study, Langmuir 36 (23) (2020) 6482–6493, https://doi.org/10.1021/acs.langmuir.0c00845.
[50] L. Zhang, P. Keblinski, J.S. Wang, B. Li, Interfacial thermal transport in atomic junctions, Phys. Rev. B - Condens. Matter Mater. Phys. 83 (2011) 1–9, https://doi.org/10.1103/PhysRevB.83.064303.
[51] B. Chen, L. Zhang, Optimized couplers for interfacial thermal transport, J. Phys. Condens. Matter. 27 (12) (2015) 125401, https://doi.org/10.1088/0953-8984/27/12/125401.
[52] C.B. Saltonstall, C.A. Polanco, J.C. Duda, A.W. Ghosh, P.M. Norris, P.E. Hopkins, Effect of interface adhesion and impurity mass on phonon transport at atomic junctions, J. Appl. Phys. 113 (1) (2013) 013516, https://doi.org/10.1063/1.4773331.